Geochemistry, Geophysics, Geosystems®

AGU ADVANCING EARTH AND SPACE SCIENCES

RESEARCH ARTICLE
10.1029/2023GC011250

Key Points:

- A two-step machine learning workflow identifies mound structures in bathymetry data and classifies their origins based on auxiliary data
- Significant increase in potential seafloor massive sulfides (SMS) edifices detected within the trans-Atlantic geo-traverse hydrothermal field distributed within latitudinal bands
- SMS mineral potential is likely lower than previously assumed due to heterogeneously distributed mineralization within mounds

Supporting Information:

Supporting Information may be found in the online version of this article.

Correspondence to:

A. Haroon,
aharoon@geomar.de

Citation:

Haroon, A., Paasche, H., Graber, S., Petersen, S., Attias, E., Jegen, M., et al. (2023). Automated seafloor massive sulfide detection through integrated image segmentation and geophysical data analysis: Revisiting the TAG hydrothermal field. *Geochemistry, Geophysics, Geosystems*, *24*, e2023GC011250. https://doi.org/10.1029/2023GC011250

Received 26 SEP 2023
Accepted 25 NOV 2023

Author Contributions:

Conceptualization: Amir Haroon, Hendrik Paasche
Formal analysis: Amir Haroon
Funding acquisition: Amir Haroon
Investigation: Amir Haroon
Methodology: Amir Haroon, Hendrik Paasche

Automated Seafloor Massive Sulfide Detection Through Integrated Image Segmentation and Geophysical Data Analysis: Revisiting the TAG Hydrothermal Field

Amir Haroon[1,2], Hendrik Paasche[3], Sebastian Graber[1,4], Sven Petersen[1], Eric Attias[5,6], Marion Jegen[1], Romina Gehrmann[7], Sebastian Hölz[1], and Meike Klischies[1,8]

[1]Helmholtz Centre for Ocean Research, GEOMAR Kiel, Kiel, Germany, [2]Hawaii Institute of Geophysics and Planetology, School of Ocean and Earth Science and Technology, University of Hawai´i at Manoa, Honolulu, HI, USA, [3]UFZ Helmholtz Centre for Environmental Research, Leipzig, Germany, [4]Helmut-Schmidt Uni Hamburg, Hamburg, Germany, [5]Institute for Geophysics, Jackson School of Geosciences, The University of Texas at Austin, Austin, TX, USA, [6]Department of Geology and Geophysics, Woods Hole Oceanographic Institution, Woods Hole, MA, USA, [7]Defence Research and Development Canada, Dartmouth, NS, Canada, [8]North.io GmbH, Kiel, Germany

Abstract Accessible seafloor minerals located near mid-ocean ridges are noticed to mitigate the projected metal demands of the net-zero energy transition, promoting growing interest in quantifying the global distributions of seafloor massive sulfides (SMS). Mineral potentials are commonly estimated using geophysical and geological data that lastly rely on additional confirmation studies using sparsely available, locally limited, seafloor imagery, grab samples, and coring data. This raises the challenge of linking in situ confirmation data to geophysical data acquired at disparate spatial scales to obtain quantitative mineral predictions. Although multivariate data sets for marine mineral research are incessantly acquired, robust, integrative data analysis requires cumbersome workflows and experienced interpreters. We introduce an automated two-step machine learning approach that integrates the mound detection through image segmentation with geophysical data. SMS predictors are subsequently clustered into distinct classes to infer marine mineral potentials that help guide future exploration. The automated workflow employs a U-Net convolutional neural network to identify mound structures in bathymetry data and distinguishes different mound classes through the classification of mound architectures and magnetic signatures. Finally, controlled source electromagnetic data are utilized together with in situ sampling data to reassess predictions of potential SMS volumes. Our study focuses on the Trans-Atlantic Geotraverse area, which is among the most explored SMS areas worldwide and includes 15 known SMS sites. The automated workflow classifies 14 of the 15 known mounds as exploration targets of either high or medium priority. This reduces the exploration area to less than 7% of the original survey area from 49 to 3.1 km^2.

1. Introduction

Over 700 active, inactive and extinct hydrothermal vent sites (cf. definitions in Jamieson & Gartman, 2020) are known to exist along mid-ocean ridges, volcanic arcs, or back-arc spreading centers (Beaulieu et al., 2015; Beaulieu & Szafranski, 2020). Their existence is documented through hydrothermal plumes that are visually confirmed using a suite of underwater-vehicles (e.g., Murton et al., 2019), towed-camera systems (Beaulieu et al., 2013), or via in situ probing such as gravity coring (Petersen et al., 2016) or seafloor drilling (e.g., Murton et al., 2019). Understanding the distributions of hydrothermal venting, often associated with the evolution of seafloor massive sulfides (SMS), remains a prevalent research topic motivated by the increased demand of strategic minerals needed to foster the net-zero energy transition. The economic and environmental challenges of modern society interface with various fields of marine research to predict where subsurface processes transport mineral-enriched high-temperature fluids from the deep lithosphere toward the seafloor. In many cases, these processes are associated with mineral accumulations that form distinct seafloor expressions (e.g., Fouquet et al., 2010) are commonly referred to as SMS mounds. Current estimates suggest that the abundance of known SMS can contribute a fractional supply of strategic metals in the future (Hannington et al., 2011), albeit there are known uncertainties with respect to size, distribution, volume, as well as the environmental impact that would pursue mining these potential deep-sea resources.

Tonnage estimates of marine minerals are interpreted from seafloor morphology (e.g., Fouquet et al., 2010; Graber et al., 2020), geophysical analyses (Galley et al., 2021; Gehrmann et al., 2019; Haroon et al., 2018;

Project Administration: Amir Haroon
Software: Amir Haroon
Supervision: Hendrik Paasche
Validation: Amir Haroon
Writing – original draft: Amir Haroon
Writing – review & editing: Amir Haroon, Hendrik Paasche

Murton et al., 2019), or global extrapolations from deposit occurrences along spreading centers (Hannington et al., 2011). Many studies have focused on previously known SMS sites and their immediate surroundings (e.g., Graber et al., 2020; Jamieson et al., 2014; Murton et al., 2019), likely leading to an underestimation of mapped SMS edifices. For example, Jamieson et al. (2014) discovered over 400 undocumented SMS edifices through manual analysis of high-resolution bathymetry data along the Endeavor Segment. These findings highlight prevalent questions concerning sampling methodologies, sampling locations, and sampling resolution. Questions are often guided by experience, funding, technological constraints and ship-time availability. Moreover, marine scientists recognize the challenges of differentiating prospective SMS mounds from morphologically comparable volcanic constructions (Jamieson et al., 2014) based on bathymetry data alone. In such cases, multivariate databases that include geophysical, geochemical, and geological data acquired across disparate spatial scales can help to (a) identify regions of interest for more detailed in situ sampling or visual confirmation studies, (b) optimize the use of ship-time through targeted surveying and (c) improve volumetric estimates of SMS candidates via integrative geophysical analyses. However, to process, analyze and interpret this mass of information, integrative data workflows are pivotal for optimally extracting valuable information, improving decision-making tools for localized sampling, and providing more rigorous estimates of known SMS provinces. Here, machine learning (ML) offers avenues to develop coherent data workflows and processing chains that are sufficiently generic and thereby transferable across various geological domains, spatial scales, and data layers. We demonstrate an ML-based workflow to automatically detect mound-like morphology on the seafloor and identify potential SMS areas based on auxiliary geological and geophysical information.

Geoscientific studies utilizing ML are progressively increasing in environmental and exploration research (e.g., Bouwer et al., 2022; Koedel et al., 2022). ML applications differ not only in the type and spatial and temporal resolution of the input data but also in the applied techniques. In marine mineral research, ML applications have applied random forest classification (e.g., Gazis et al., 2018) or neural networks (e.g., Juliani & Juliani, 2021; Keohane & White, 2022), focusing mainly on one or two types of input layers (e.g., seafloor images and/or bathymetry data). However, as interdisciplinary SMS databases grow via contributions from geological, geophysical (e.g., Müller et al., 2023), biological and geochemical applications, ML workflows are expected to also evolve into more generic implementations to facilitate this growing demand of interdisciplinary marine research.

Our study leverages previous ML applications conducted in the marine environment. We introduce a workflow that integrates concurrent data acquired at different spatial scales to better describe the mineral potential within the Trans-Atlantic Geo-traverse (TAG) hydrothermal field. The TAG field is one of the most studied SMS sites and various data sets are available, thus suitable for our proposed validation study. First, a modified approach adapted from Juliani and Juliani (2021) is utilized to identify mound structures in bathymetry data using a U-Net convolutional neural network. Subsequently, identified mound contours are amalgamated with multivariate geophysical and geological data to provide a more rigorous identification of potential SMS edifices. We test the developed workflow using data described in Petersen et al. (2016) and Murton et al. (2018) acquired during two expeditions conducted at the TAG hydrothermal field within the framework of the Blue Mining project (https://bluemining.eu/). This study extends previously published concepts of ML applications in marine mineral research by including more diversified, multivariate input layers such as reduced-to-the-pole (RTP) magnetics, controlled source electromagnetic (CSEM) data, transient electromagnetic (TEM) data, and core/grab samples, all acquired across various spatial scales of resolution.

2. Geological and Geophysical Data

The data used in this study were previously published in the scientific literature, that is, Petersen et al. (2016), Murton et al. (2018), Szitkar et al. (2019), Haroon et al. (2018), Gehrmann et al. (2019), Graber et al. (2020),s Gehrmann et al. (2020), Galley et al. (2021). The following describes relevant aspects of the data that are needed in the context of the ML implementation. Details on data acquisition and geological/geophysical interpretations are found within the above-mentioned literature. It is important to note that from a data science perspective, the available data introduce *a-priori* bias as these were acquired with the specific purpose of imaging certain physical parameters that, from a geological perspective, are associated with the evolution of SMS. Thus, unknown correlations that extend beyond the current geological understanding of SMS evolution are likely neglected in the presented ML workflow.

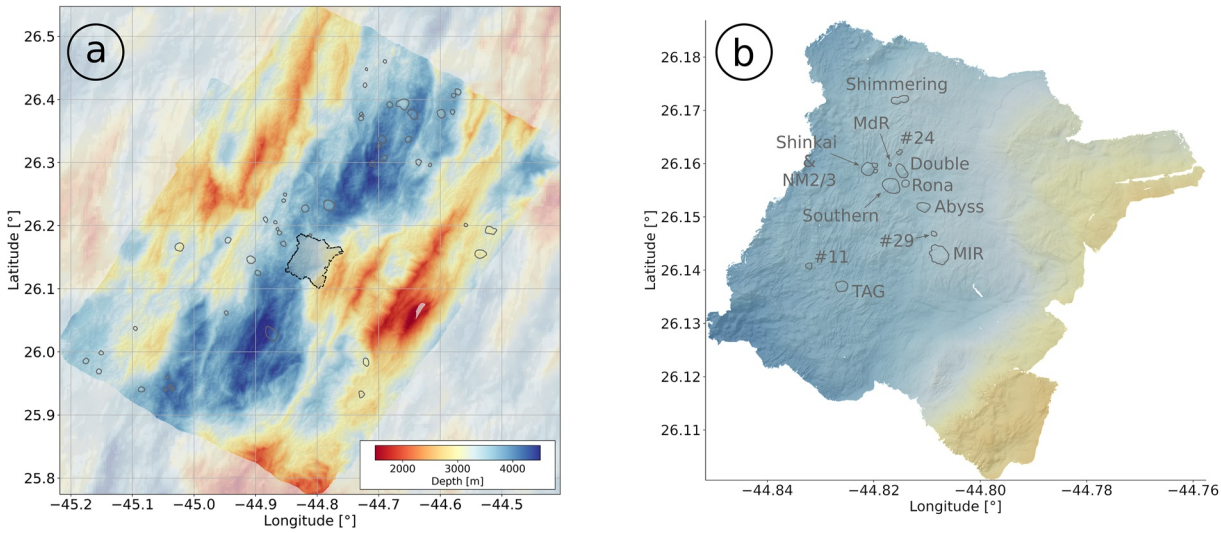

Figure 1. Bathymetry maps of the study area. (a) The General Bathymetric Chart of the Oceans (GEBCO) bathymetry (shaded map) overlain by the ship-based bathymetry data acquired during Research Vessel (RV) Meteor cruise M127 with a spatial resolution of 30 m. Gray outlines denote visible mound structures, whereas the black outlined region denotes the high-resolution bathymetry survey illustrated in panel (b). (b) autonomous-underwater vehicle bathymetry data acquired with a spatial resolution of 2 m using the same color scale as in panel (a). Known seafloor massive sulfides mounds are outlined and labeled as depicted by Graber et al. (2020).

2.1. Bathymetry Data

Seafloors host numerous focused on fluid discharge sites that can appear as mounded manifestations in the seafloor topology (Olakunle et al., 2021). Linking these manifestations to either a volcanic or hydrothermal origin based on structural differences (cf. Jamieson et al., 2014) or observations of physical parameters (i.e., magnetic anomaly, conductivity, self-potential, etc.) and deriving their potential for forming metalliferous accumulations requires auxiliary data acquired at each specific site. The high-resolution seafloor bathymetry data provide a spatial baseline of where to sample for potential SMS occurrences and also the structural framework for volumetric predictions (e.g., Graber et al., 2020; Jamieson et al., 2014).

High-resolution bathymetry data used for image segmentation were collected during research cruise M127 (Research Vessel (RV) Meteor, 2016) using ship-based multibeam (Figure 1a) and GEOMAR's Autonomous-Underwater Vehicle (AUV) Abyss (Petersen et al., 2016). AUV bathymetry data were acquired using a RESON Seabat 7125 multibeam echosounder, navigated at a speed of three knots using a frequency of 200 kHz. The line spacing between adjacent profiles was between 80 and 100 m at an average altitude of 84 m relative to the seafloor, resulting in a 2 m grid resolution (Figure 1b). The bathymetry data were processed using the software package MB Systems (https://www.mbari.org/technology/mb-system/) and geo-referenced based on prominent seafloor features (Graber et al., 2020; Szitkar et al., 2019). This high-resolution bathymetry constructs the baseline of positioning morphological structures during automated segmentation.

To further optimize the U-Net model, we utilize available high-resolution AUV bathymetry data acquired at different SMS sites around the globe (e.g., Clague et al., 2015; Escartín & Petersen, 2017) and other openly-available ship-based bathymetry data. All of the bathymetry grids utilized to train, validate and test the U-Net model are listed in Table A1.

2.2. AUV-Based Magnetic Data

Magnetic properties of seafloor basalts are dictated by two alteration processes, namely deuteric oxidation during the initial cooling phase and the superimposed regional hydrothermal alteration that occurs at younger ages (Ade-Hall et al., 1971). During the latter process, high-temperature fluids can cause permanent demagnetization of basalt due to the alteration of titanomagnetite (Szitkar et al., 2019). Thus, RTP magnetic lows constitute a meaningful geophysical exploration criterion for the recognition of high-intensity hydrothermal discharge zones and potential SMS deposits in the TAG region (Rona, 1978, 1980).

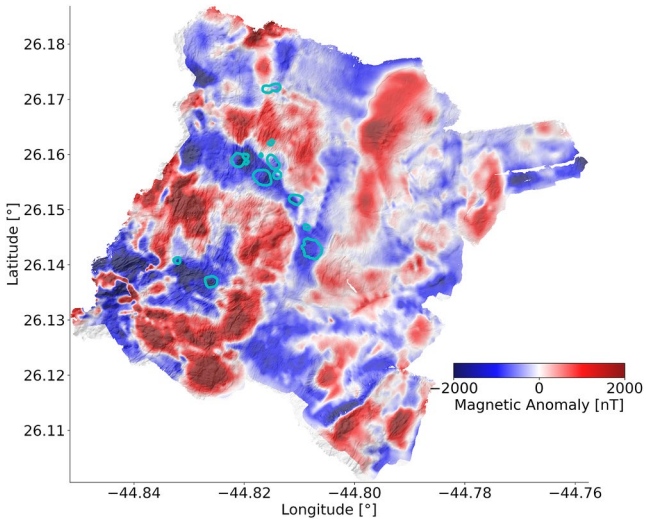

Figure 2. Overlay map of the hillshade bathymetry (2 m resolution) and the magnetic anomaly map with 10 m spatial resolution from Petersen (2019). Outlined in black are the known seafloor massive sulfides mounds depicted by Graber et al. (2020).

During M127, the AUV Abyss was augmented by an applied physics system 1540 digital three-axis miniature Fluxgate-magnetometer recording at 10 Hz. At the time of the cruise, the Earth's inducing field vector had an inclination of 42°, declination of −15°, and field strength of about 38290 nT (Galley et al., 2021). Induced and permanent magnetization effects caused by the AUV itself were removed from the magnetic data by conducting figure-eight calibration dives to solve for the AUV's magnetic properties following Honsho et al. (2013). The magnetic data illustrated in Figure 2a have been interpreted regionally by Szitkar et al. (2019) and locally around the TAG mound by Galley et al. (2021), and are openly available as a 10 m raster (Petersen, 2019).

AUV drift leads to indeterminate errors that may propagate into the workflow. Using an inertial system, the AUV's lateral position is tracked from the initially calibrated position. However, water column currents may induce gradual shifts away from the inferred position. In comparison to the vertical position of the AUV that is determined through altimeter and depth readings, a lateral shift between the magnetic anomalies and bathymetric features can either be geology driven (cf. Szitkar et al., 2019) or, alternatively, result from positioning errors; both are relevant constraints for the data integration process of the described ML workflow and are addressed in Section 3.3.

2.3. Electrical Conductivity

Accumulations of SMS exhibit a distinct contrast in the electrical resistivity compared to the surrounding basalt (Morgan, 2012; Spagnoli et al., 2016). Sulfide mounds are generally more porous compared to the background basalt (Murton et al., 2019), host high-temperature fluids when active, and contain metalliferous minerals and clays, all attributes that contribute to a decrease in electrical resistivity. Several electromagnetic (EM) applications have been proposed to detect and characterize volumes of minerals, for example, at TAG (Gehrmann et al., 2019; Haroon et al., 2018) or in the Okinawa Trough (Constable et al., 2018; Ishizu et al., 2019; MacGregor et al., 2021).

2.3.1. Controlled Source Electromagnetic Measurements

CSEM data were acquired using two fixed-offset Vulcan receivers (Constable et al., 2016) towed at distances of 350 and 505 m behind a 50-m horizontal electric dipole source (Sinha et al., 1990). The resulting 2D resistivity models computed with MARE2DEM (Key, 2016) are interpreted and discussed by Haroon et al. (2018) and Gehrmann et al. (2019, 2020). In summary, the CSEM conductivity models highlight distinct regions of known SMS through decreased electrical resistivity. Here, we use the acquired CSEM data to reassess the electrical resistivity distributions at potential SMS sites. Additionally, electrical conductance illustrated along CSEM profiles in Figure 3a is used to qualitatively define spatial extents of conductive, possibly mineral-enriched seafloor, and predict if morphological expressions are associated with hydrothermal (conductive) or volcanogenic (resistive) activity. For each profile, the conductance is calculated as the integrated conductivity-thickness product for 5-m intervals from the seafloor down to the depth where resistivity increases to above 1 Ωm (Gehrmann et al., 2019).

2.3.2. Transient Electromagnetic Measurements

Marine TEM data were acquired at two specific sites within the TAG hydrothermal field using GEOMAR's MARTEMIS system (Figures 3b and 3c). The system consists of one transmitter loop and one coincident receiver loop, which are housed in a 6.3 × 6.3 m^2 frame. The system is towed 5–15 m above the seafloor at <1 knot and records the EM response of a 50% duty-cycle transmitter signal at 10 kHz sampling rate. The acquired time series are processed considering the distorting effects described by Reeck et al. (2020) and transformed into full-space apparent conductivity curves following Equation 1 of Haroon et al. (2018). Regions of increased apparent conductivity are generally associated with areas where the seafloor is less resistive than the seawater resistivity ($\rho < 0.33$ Ωm), which in our setting is indicative of hydrothermal activity (Swidinsky et al., 2012), that is, increased mineralization or increased pore fluid temperatures. MARTEMIS positioning was obtained through an ultra-short baseline transponder attached to the tow cable and merged with the processed apparent conductivity data. The spacing between adjacent stations is approximately 10 m (Figures 3b and 3c).

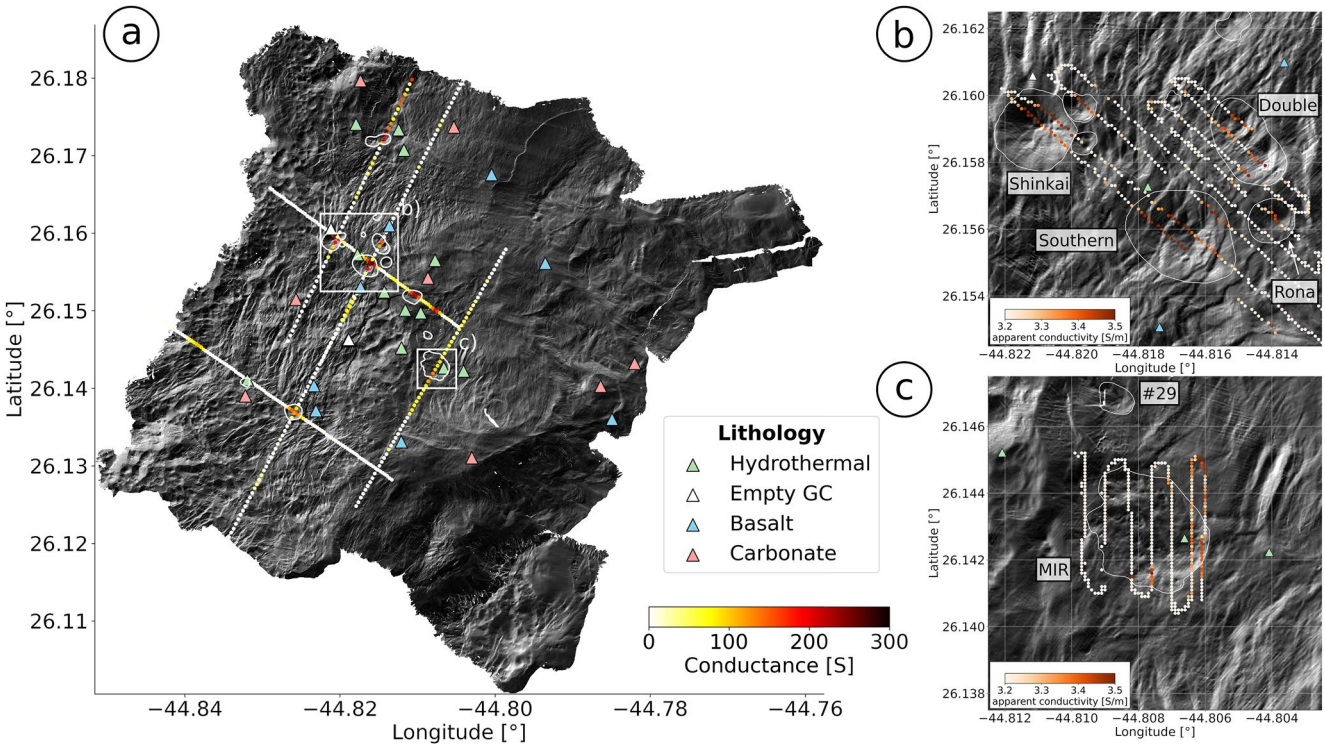

Figure 3. (a) Hillshade map of the bathymetry data with a spatial resolution of 2 m. Computed electrical conductance values derived from 2D controlled source electromagnetic (EM) resistivity models of Gehrmann et al., 2019 are displayed with color-coded markers. Light colors denote low and hot colors a high conductance. (b) Zoom-in of the Three-Mound region overlain by the transformed apparent conductivity values obtained by transient EM measurements. (c) Same as panel (b) but for the MIR zone. Outlines of the mounds denote the manually-labeled lateral mound dimensions from Graber et al. (2020). Triangular markers in panels (a) through (c) illustrate the locations of the 3 m gravity cores and the lithology observed within the core samples (Petersen, 2019).

2.4. In-Situ Data

Overall, 33 gravity cores of max. 3-m length were acquired within the TAG hydrothermal region during M127 (Petersen et al., 2016). Locations of possible coring sites were selected with the help of the high-resolution AUV bathymetry data. Twenty-three cores contained abundant sediment, eight contained only fragments of gravel, basalt and traces of sediments in the core catcher, and two were empty (Figure 3, white markers). Among the 23 sediment cores, 10 had visible hydrothermally-influenced indications (Figure 3, green triangles); the other cores had the visual appearance of background sediments (carbonate ooze) or showed layers of volcanic origin (Figure 3, red and blue triangles, respectively). Note that background sediments or empty cores do not rule out hydrothermal activity at greater depths, as the penetration of this coring experiment was limited to a maximum of three m below the seafloor.

In addition to gravity cores, rock drill samples were drilled to a maximum depth of 12.5 m below the seafloor (Murton et al., 2019). The obtained samples from the Southern, Rona and MIR mounds (location shown on Figure 1b) show high concentrations of minerals, confirming the hydrothermal origin of these three mounds. Here, we link core sites indicative of hydrothermal alteration with collocated EM resistivity data and models to evaluate spatial extents of mineralization on these mounds to reassess existing mineral potentials.

3. Methods

The workflow is split into four steps as illustrated in Figure 4: (a) selecting and preparing suitable mid-ocean ridge bathymetry data from accessible open-source data repositories (Table A1) and manually labeling mounds using shapefile polygons in QGIS, (b) training, validating and testing the U-Net model, (c) post-processing of the model output to derive mound architectures and integrate with concurrent RTP magnetic data, and (d) classification and geophysical analysis of identified mounds. The workflow is scripted in Python (Ver. 3.8.12) and uses the TensorFlow (Ver. 2.4.1) and Scikit-Learn (Ver. 1.0.2) libraries.

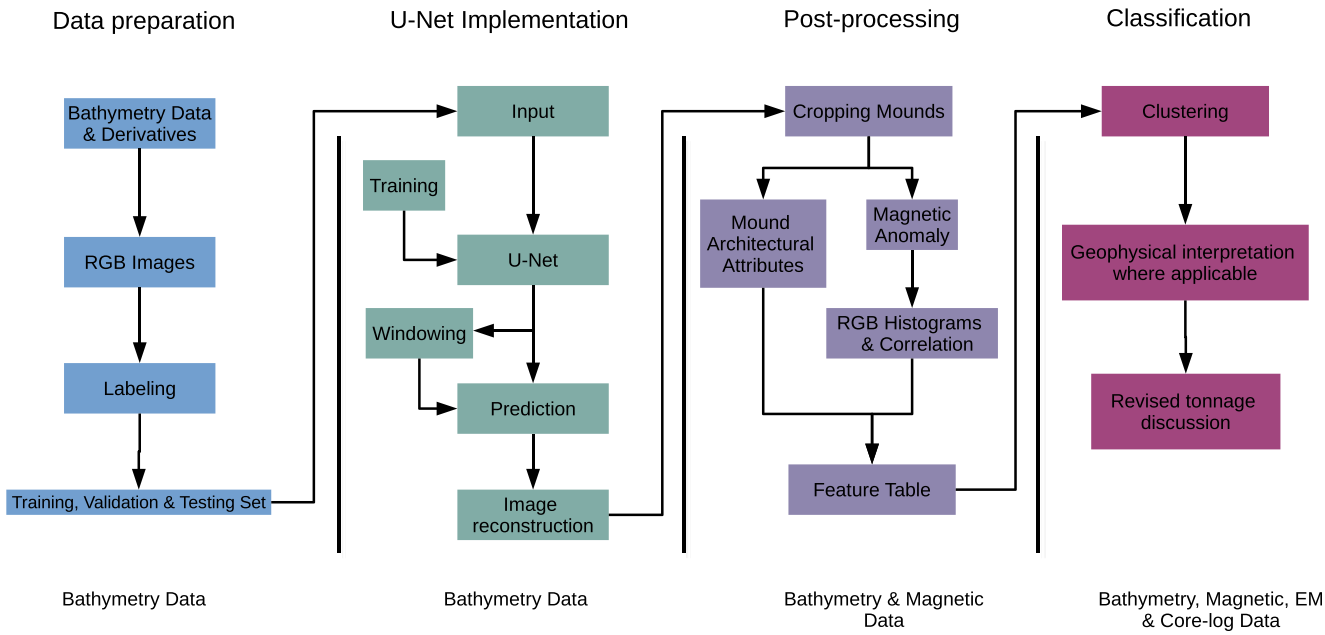

Figure 4. Schematic of the applied workflow including all relevant steps applied, that is, data preparation, U-Net implementation, post-processing and classification.

3.1. Data Preparation: Bathymetry Data

Bathymetry data used for training, validation and testing are identified as suitable if a large spatial coverage was acquired at either MORs or at specific hydrothermal fields. Each bathymetry raster was manually labeled using shapefile polygons in QGIS, where pixels within each polygon were labeled as *True* and all other pixels were labeled as *False*. The utilized bathymetry data are listed in Table A1.

A common standard of visualization which highlights rounded convex and concave morphology through distinct representations is achieved through a multi-directional slope analysis. The normalized aspect, slope, and the ∂y derivative are mapped onto Red, Green and Blue channels of a standardized Red Green Blue (RGB) image, respectively (Figure 5). Converting certain derivatives of bathymetry data into single RGB images facilitates a generalized visual interpretation and aids the model performance. All resulting images show the northern mound

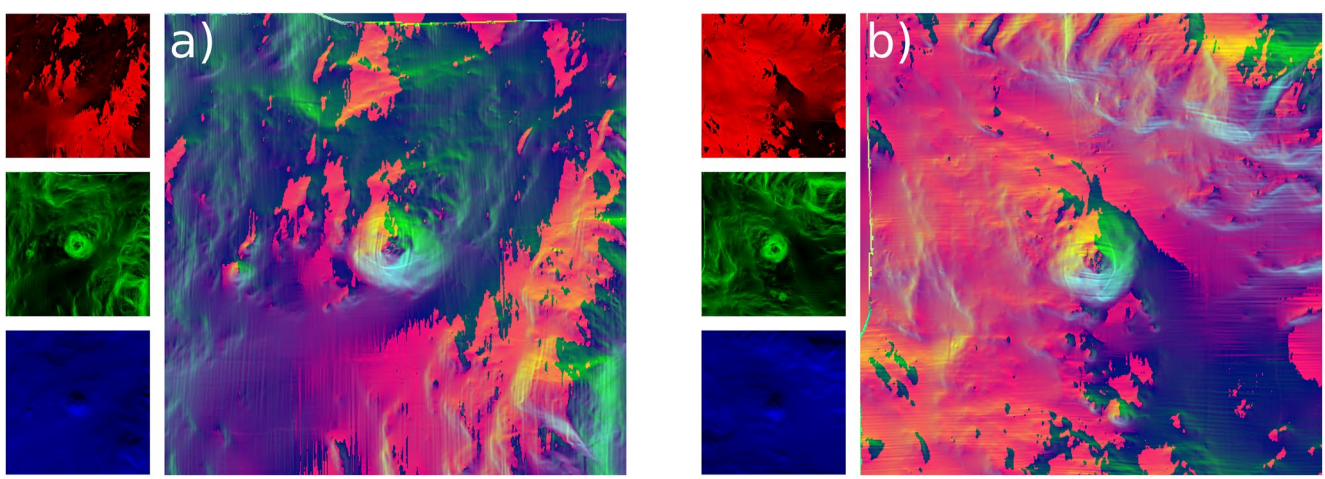

Figure 5. Image unification example of relevant bathymetry features into a common visual representation that is generically applicable to coherently address bathymetry data acquired at different regions across the globe. The aspect, slope, and ∂y derivative of the bathymetry are mapped onto the red, green and blue channels of a standardized 0–255 RGB image (left column of each panel). In this representation, mounds appear directionally invariant with coherent color representation. (a) Original input data and (b) the original input data rotated by 90°. Contrarily, the background bathymetry differs based on the predominant strike direction of the seafloor morphology, whereas prominent mound features remain rotationally invariant.

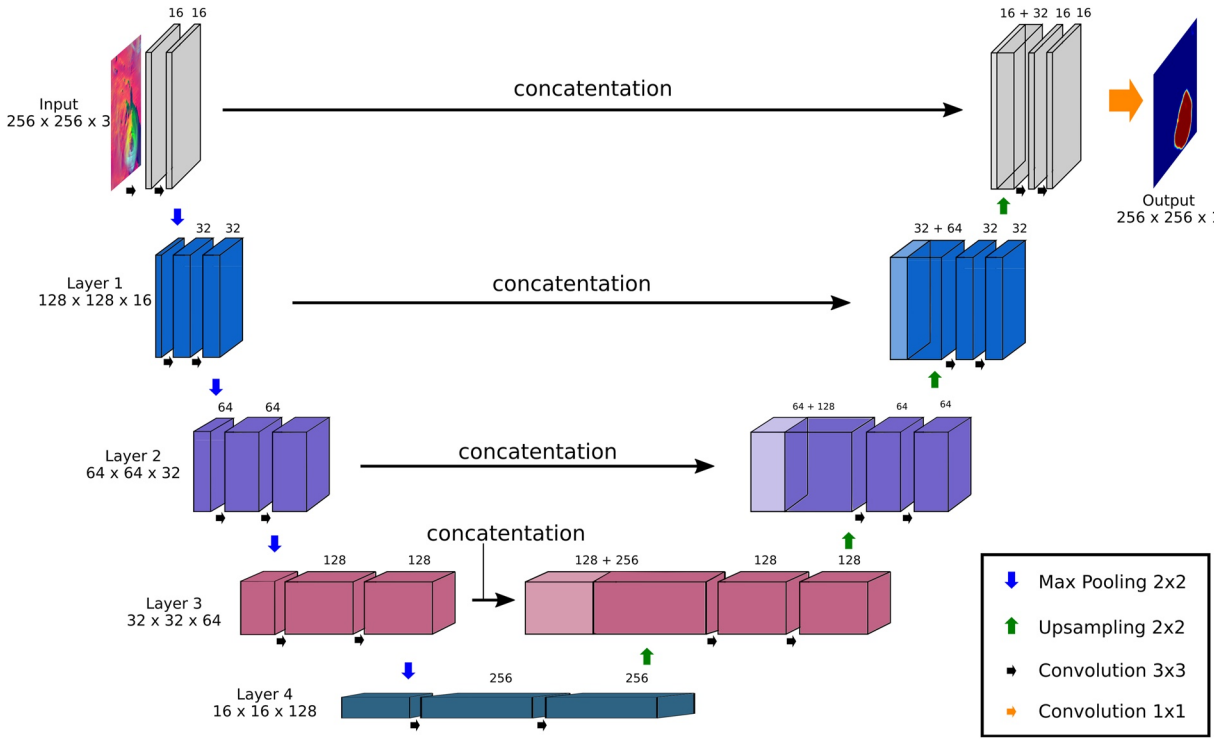

Figure 6. Schematic of the U-Net architecture used for semantic segmentation of the bathymetry data (modified after Ronneberger et al., 2015).

flank in yellow to green moving west to east. Southern flanks appear white to blue. Concave features such as pits appear in a reversed manner.

During data preparation, directional dependencies of background features in the preprocessed bathymetry images remain unaltered (Figure 5). To increase the amount of training data and mitigate undesired learning of directional dependencies, input bathymetry was augmented by means of a 90° rotation (cf. Mikolajczjk and Grochowski (2018) for examples of image augmentation in deep learning). As mound structures are near-circular structures, they remain rotationally invariant although background strike differs (cf. Figures 5a and 5b). After each bathymetry raster was transformed into the common visualization, the rasters and label maps were subdivided into overlapping image patches of 256 × 256 pixels with a step length of 128 pixels. In total, 2,280 RGB image patches were produced to train, validate and test the U-Net model, each consisting of 65,536 pixels.

3.2. U-Net Implementation, Training and Evaluation

The model architecture yields an end-to-end trainable neural network including segmentation of input images into partitioned pixel sets of corresponding classes. This type of network was first introduced for biomedical image segmentation by Ronneberger et al. (2015) and resembles a symmetric "U" (Figure 6). In our specific case, the U-Net model distinguishes a mound from background features and provides values of probabilities as outputs (Hu et al., 2015).

For training, validating and testing, only images containing at least two percent labeled mound pixels were considered. The data set was split into subsets where 75% was used for training, 20% for validation and 5% reserved for testing. We used the binary cross-entropy loss function defined as

$$H_p(q) = \frac{1}{N}\sum_{i=1}^{N} y_i \cdot \log(p(y_i)) + (1 - y_i)\log(1 - p(y_i)) \quad (1)$$

where y_i refers to the corresponding binary label of each pixel and $p(y_i)$ to the predicted value between 0 and 1 within each epoch i of training. The accuracy, true positive and false negative metrics were computed to determine a point of early stopping, that is, a model with sufficient accuracy and minimal over-fitting (Figure 7). The model predictions are contoured at values of >0.5 to outline the lateral dimensions of mound pedestals.

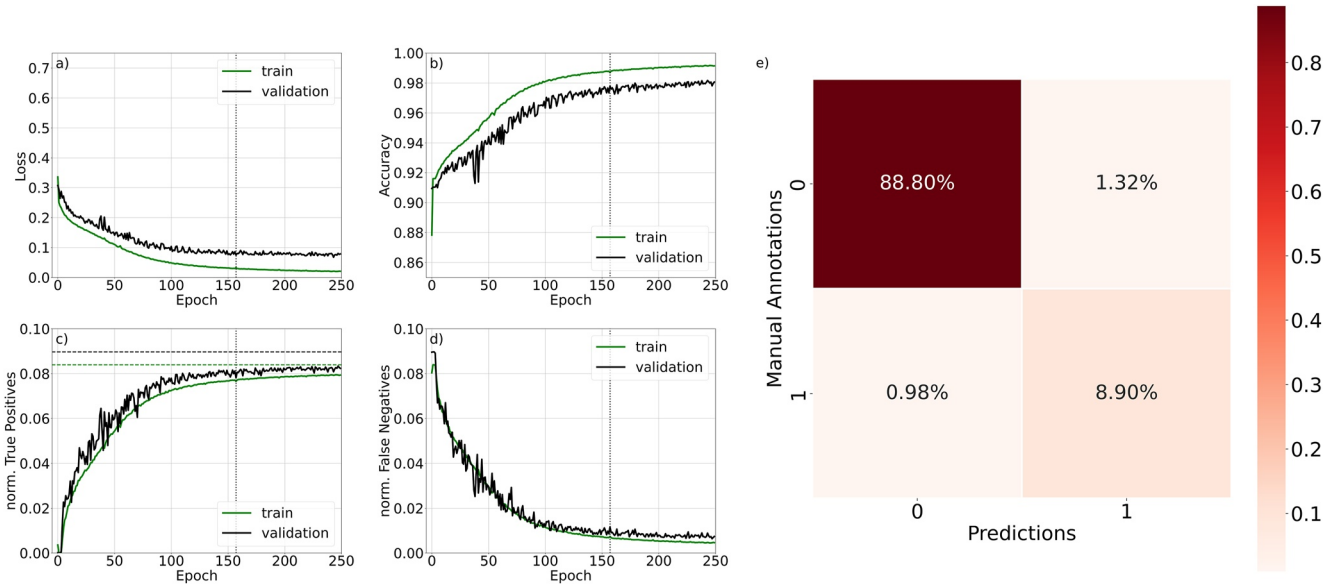

Figure 7. (a) Binary cross-entropy loss function used during training (green) and validation (black). Additional metrics, that is, (b) accuracy, (c) true positives, and (d) false negatives are also used to assess the model performance. Note that true positives and false negatives are normalized to represent percentages of pixels per image. The vertical dotted line denotes the point of early stopping, whereas the horizontally dashed lines in (c) represent the average number of pixels affiliated with the mound structure within the training and validation data. (e) Confusion matrix computed for the test data to further illustrate the model performance for unseen images.

After training, the pre-processed AUV bathymetry from the TAG area is presented to the U-Net model as overlapping patches of 256 × 256 pixels. The image reconstruction process is illustrated in Figure 8. To prevent inaccurate predictions along the patch edges, an image smoothing considers only the central 128 × 128 pixels. The outer edges of each predicted patch are neglected. Using an overlapping process, each pixel of the bathymetry grid is included four times within the output prediction. The maximum probability from the four predictions is used as the final pixel probability.

3.3. Post-Processing of Mound Structures

The predicted contours define the location and lateral footprints of each mound in m^2. A minimum footprint threshold of ~1,040 m^2 (290 pixels) is introduced to (a) remove most of the falsely detected mound structures

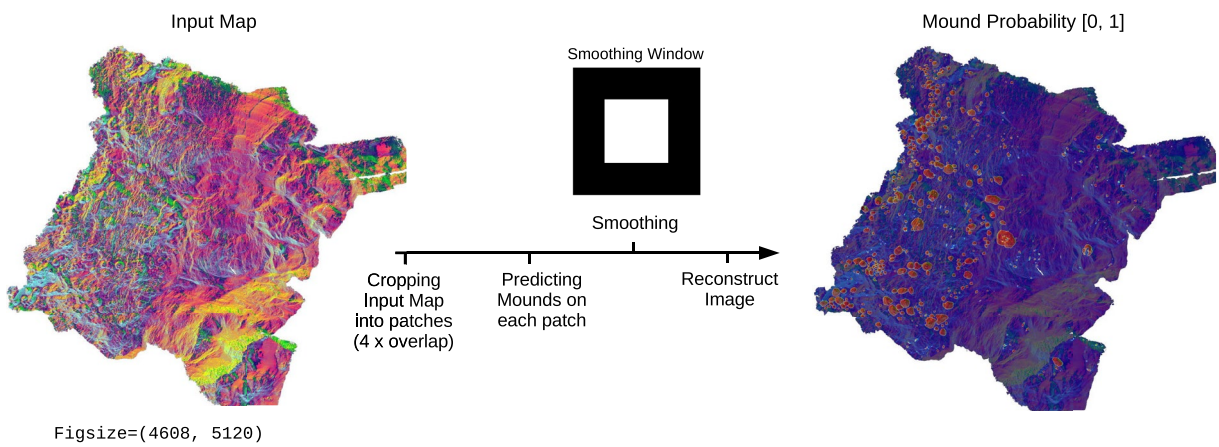

Figure 8. Workflow of mound prediction for the autonomous-underwater vehicle (AUV) bathymetry raster. The pre-processed AUV bathymetry map is cropped into overlapping 256 × 256 patches, which are presented to the U-Net for prediction. The output is smoothed using a displayed window where pixels within the black region are neglected due to edge effects that deteriorate predictions (as observed within the testing phase). The right panel shows the final prediction map that is utilized for further processing.

Table 1
Metrics and Corresponding Benchmarks of the Applied U-Net Model for Training, Validation and Testing Images

Metric	Training		Validation		Test	
Accuracy	Benchmark: 0.91603 Prediction: 0.98696		Benchmark: 0.9103 Prediction: 0.97790		Benchmark: 0.89777 Prediction: 0.976976	
True Positives	Benchmark: 0.08397 Prediction: 0.07659	91.2%	Benchmark: 0.08970 Prediction: 0.07816	87.1%	Benchmark: 0.10223 Prediction: 0.088996	87.1%
False Negatives	Prediction: 0.00738		Prediction: 0.01154		Prediction: 0.01323	

Note. Benchmark refers to the starting condition where all pixels of each image are predicted as false, that is, not belonging to a mound.

caused by geological noise and (b) focus the analysis on potentially significant SMS volumes (cf. Murton et al., 2019). We compute the lateral footprint, maximum height, and median slope of each mound using only pixels located within each contour. These parameters describe the general mound architecture and serve as input parameters for classification.

For integrating the magnetic anomaly data with the detected mounds from the U-Net, an image overlay of gray-scaled hillshade and a diverging red-to-blue magnetic anomaly map (Figure 2) is cropped and centered around each mound, including also peripheral areas. Using the specific red-blue color representation, RTP anomalies appear either red (if positive) or blue (if negative), both being primary color channels within an RGB color spectrum. Color histograms and correlations of the three RGB channels depict positive, negative or a mixture of RTP anomalies into three single values, depending on whether the image is blue, red, or a blue/red blend. The channel correlations serve as further input parameters for the subsequent classification of the mounds.

3.4. Classification and Evaluation

We applied spectral clustering using the Scikit Learn Python Library to the derived parameters for each mound contour. Where available, we added auxiliary SMS indicators derived from gravity cores, EM data and known SMS edifices to determine mound evolution and assess the mineral potential at confirmed high-priority sites. Defined simply as those sites classified within the cluster that contains most of the known SMS mounds. The ensemble of spatially distributed morphological expressions and geological/geophysical characteristics is used to geologically describe the formation and distribution of SMS mounds in the TAG hydrothermal field. Further, it provides the basis to rediscuss the resource potential of the TAG field.

4. Results

4.1. U-Net Analysis

The U-Net was trained on a Fujitsu Lifebook U Series and each training epoch took approximately 8 min and 20 s. Computed metrics indicate an optimal point of early stopping at epoch 158 (Figure 7). There, the network reached a prediction accuracy of greater than 98.6 and 97.8% in training and validation, respectively (cf. Table 1). The training loss reached 0.032 and the validation loss 0.075 using a learning rate of 10^{-4}. A learning trend is observable in the ensuing epochs, especially within the training data. However, the trend is less pronounced within the validation data, indicating that predictions will perhaps not improve for unseen images.

Based on the manual labeling, mound structures make up, on average, less than 8.2 and 9.1% of the total pixels in each of the training and validation images, respectively. This significant imbalance compared to background leads to a high starting accuracy of approximately 91%, assuming that all pixels are predicted as background, that is, 0 or *False*. Metrics such as true positives and false negatives are more expressive for these imbalanced scenarios. At the point of early stopping, the trained network retrieves 87% of the true positive pixels in the validation data, meaning that manually labeled mounds are also classified as such by the U-Net. Similarly, false negatives are minimized to less than 1% of the total pixels per image in both training and validation sets, indicating that only a few background formations are being falsely classified as mounds.

In addition to the metrics derived from the training and validation data, 114 images were reserved as a test subset to further assess the U-Net's efficiency and prediction characteristics for unseen images. A confusion matrix

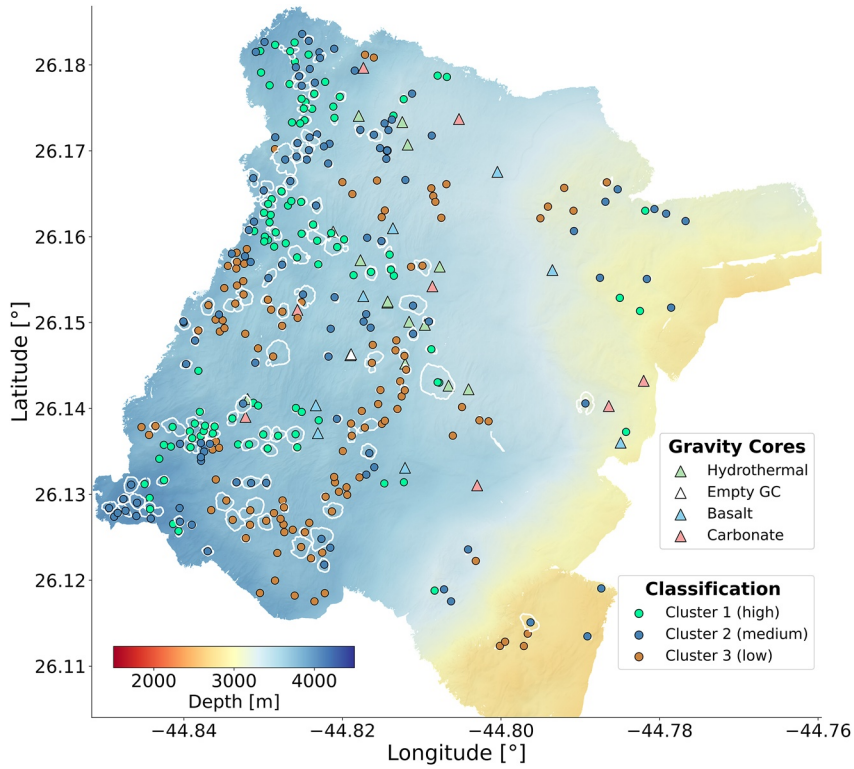

Figure 9. Bathymetry map containing the 323 mounds with a lateral footprint greater than 290 pixels (1,040 m^2) as predicted by the U-Net. The mounds are illustrated by white contours and classified as either Cluster 1 (high priority), Cluster 2 (medium priority), or Cluster 3 (low priority). Dotted gray lines illustrate the interpreted boundaries of the three latitudinal bands containing hydrothermal edifices.

(Figure 7e) computed for this test set illustrates that the majority of pixels for unseen images are correctly classified as either true positives (8.9%) or true negatives (88.8%) and less than 2.3% of the total pixels are incorrectly classified as either false positives (1.32%) or false negatives (0.98%).

There is some bias to consider in the evaluation of pixel-based metrics. Discrepancies in mound dimensions between manual labeling and U-Net prediction will reduce model performance and appear as either false negative or false positive in the confusion matrix, although a mound is essentially detected by the network. In the majority of studied cases within the test data, mounds were detected at the correct locations but slight differences exist between manual labeling and U-Net prediction in terms of lateral contours (cf. Figure S1 in Supporting Information S1).

The trained U-Net detects a total of 323 mounds within the mapped 49 km^2 of the AUV bathymetry data (Figure 9), each with a lateral footprint greater than 1,040 m^2 (=290 pixel). The predictions include all previously identified SMS mounds of Graber et al. (2020) (cf. Figure 1 and white outlines in Figure 9). The lateral mound dimensions qualitatively match, in most cases, the manual annotations. However, the U-Net model underestimates the spatial footprint for both Southern and Double Mounds. These mounds show a tectonized surface texture deviating from an idealized mound shape, which may explain the reduced prediction performance. Note that compared to the 14 depicted mounds in Graber et al. (2020), the total number of known mounds here accumulates to 15 because Double Mound is predicted as two individual edifices by the U-Net.

The predicted mounds can be clustered into three distinct classes (Figure 9). Table 2 lists the basic statistics for mounds of each cluster, including the minimum, maximum, and mean mound dimensions. The number of known SMS sites within each cluster defines the priority in terms of SMS potential. Cluster 1 is assigned a “high” priority as 10 out of 98 mounds are confirmed to host SMS. A “low” "SMS priority is assigned to Cluster 3, which contains only 1 confirmed SMS site out of 114 mounds, and a “medium” priority is assigned to Custer 2, where 4 known SMS sites exist out of 111 mounds.

Table 2
Clustering Statistics of Output Mounds, Including the Total Area of all Mounds and Associated Mound Dimensions

Cluster # (SMS priority)	Number of mounds	Number of known SMS sites per cluster	Total area of all mounds	Footprint	Height
1 (high)	98	10	982,314 m^2	Max: 141,310 m^2	Max: 58.62 m
				Min: 1,052 m^2	Min: 1.35 m
				Mean: 10,024 m^2	Mean: 14.46 m
2 (medium)	111	4	1,188,213 m^2	Max: 78,268 m^2	Max: 52.53 m
				Min: 1,205 m^2	Min: 0.35 m
				Mean: 10,704 m^2	Mean: 14.98 m
3 (low)	114	1	942,423 m^2	Max: 75,269 m^2	Max: 56.34 m
				Min: 1,094 m^2	Min: 1.12 m
				Mean: 8,266 m^2	Mean: 13.62 m
Total	323	15	3,112,950 m^2		

Note. The number of known SMS sites associated with each cluster defines the SMS priority of the cluster.

The clustering is primarily driven by the magnetic anomaly data (cf. Figures S2 and S3 in Supporting Information S1); SMS sites that fall within Cluster 1 show a distinct negative magnetic anomaly. Known SMS sites that exist in Cluster 2 show both positive and negative RTP magnetic anomalies. Cluster 3 contains only one previously known SMS site (Mound #24 from Graber et al., 2020) that is one of the smallest known SMS edifices in the area and associated with a positive magnetic anomaly. Images of all clustered mounds are displayed in Figure S2 in Supporting Information S1.

In contrast to the magnetic signature, mound morphology is similar in all clusters with respect to their height and mound footprints (cf. Table 2). Other morphological features potentially indicative of hydrothermal activity, such as jagged contours and number of peaks (Jamieson et al., 2014), could not be identified by our workflow as important parameters for differentiating between volcanic and hydrothermal mounds in the TAG area. This leaves the magnetic anomaly as the strongest spatial indicator in the available data set.

4.2. Spatial Distribution of Morphological Features and Magnetic Footprint

The high-priority sites (Cluster 1) occur spatially confined in three bands (labeled Southern, Central and Northern Band in Figure 9). All bands strike northwest-southeast (NW-SE), roughly perpendicular to the axis of the Mid-Atlantic Ridge, and coincide well with interfaces between different structural domains identified by Graber et al. (2020). The southern band lies within a region of oblique faults and fissures (Figure 8 of Graber et al., 2020), that have been suggested to promote upward migration of hot fluids at TAG and other regions (Andersen et al., 2015). The central band of mounds is located within the NW-SE extension of the so-called Three-mound area (cf. Graber et al., 2020), which runs parallel to mapped corrugations, and connects the Three-Mound regions to the MIR zone (Figure 9). The northern band lies north of a zone with chaotic seafloor morphology and positive magnetic signature, separating the smooth bathymetry and negative anomalies of the central and northern bands.

The alignment of Cluster 1 mounds is interrupted in several locations. In the southern band, at around 26.138°N and 44.837°W, Cluster 1 mounds are not associated with oblique fissures mapped by Graber et al. (2020). Instead, negative magnetic anomalies correlate with "fresh" pillow mounds. Such potentially younger magmatic features may mask the oblique fissures typical for the southern band. The northern band contains only one known hydrothermal site named Shimmering, but multiple gravity cores indicate an abundance of hydrothermally-altered sediments in the area (cf. Figure 9). However, mounds located at the western section of the northern band are structurally interpreted as pillow mounds (Graber et al., 2020).

4.3. Analysis Using Electromagnetic Data

SMS potentials have often assumed homogeneously distributed metal grades across a mounds morphological footprint and its corresponding stockwork zone. Although tonnage estimates are often based on in situ measurements

(i.e., core-log data/seafloor drilling), derived mineral potentials remain poorly constrained because in situ data are (a) available at only few representative mounds, (b) generally obtained at the points of highest interest, that is, where SMS is apparent in seafloor imagery and (c) penetrate only a few meters into the subsurface. In the majority of cases, the structural heterogeneity of individual mounds is either neglected or perhaps considered too simplistic, assuming that high metal grades are distributed across the entire lateral mound extension. To constrain these rather general regional mineral estimates, resistivity models derived from CSEM or TEM data may help to better understand the degree of mineralization away from the point-scale core-log observations.

Here, we focus on the EM data acquired only along high-priority mounds (Cluster 1) or verified mounds from preceding literature (e.g., Graber et al., 2020). Recomputed CSEM resistivity models at Cluster 1 mounds are illustrated in Figure 10 using data acquired by Gehrmann et al. (2019). All presented resistivity models achieve a target root mean square (RMS) = 1, using the error considerations of Gehrmann et al. (2020). Note that we only consider those mounds that are intersected by CSEM transects. Regions of low resistivity are illustrated by red to orange coloring and background resistivity through green and blue coloring.

The CSEM resistivity models illustrate that the investigated Cluster 1 mounds are generally associated with a distinct low-resistivity anomaly of variable magnitude. This, together with identified SMS in core-log data and grab samples (Murton et al., 2019; Petersen et al., 2016), confirms a certain degree of mineralization at each of the respective SMS sites. It needs to be noted that in a few instances CSEM data have only limited resolution due to the large vertical offset between the measurement system (denoted by black markers) and the seafloor (Figures 10d and 10g). Thus, limiting the spatial analysis of resistivity structure using CSEM data.

Overall, regions of decreased resistivity are generally confined to areas within the mound dimensions. Shinkai and Southern mounds, residing in the central band (Figures 10c through 10e), exhibit a relatively homogeneous low-resistive structure. This is confirmed by the apparent conductivity values ranging between 3.2 and 3.5 S/m observed across their entire lateral footprint (cf. apparent conductivity data in Figure 3b), suggesting that previous mineral estimates of these two mounds could be accurate. Contrarily, Double and Rona (Figure 3b) exhibit an apparent conductivity anomaly only in the vicinity of their summits with no notable contrast to the background at their pedestals. Although, Rockdrill cores of up to 12 m acquired at Rona's summit confirm high metal concentrations within a sulfide layer (Murton et al., 2019), TEM data indicate that the majority of Rona's volume is of lower economic value due to the lack of an apparent conductivity anomaly (Figure 3b).

MIR has the largest spatial footprint of Cluster 1 mounds in the study area (Figure 10f). Previous mineral predictions based on mound volumes and extrapolated metal grades derived from gravity cores and rock drill data suggest MIR to be the most economical site within the TAG hydrothermal field (Graber et al., 2020). The CSEM resistivity model of MIR illustrated in Figure 10f shows an irregular distribution of low-resistive zones across the mound transect that combined with the coring data indicate the presence of mineralized material but not in the quantity suggested by previous studies. The TEM data acquired along multiple transects across MIR support this inference (Figure 3c), contradicting the notion of MIRs exceptionally high mineral potential. The point-scale gravity core and Rockdrill data (Murton et al., 2019; Petersen et al., 2016) were acquired in the northwestern region of MIR, where high apparent conductivities exist. Most of the remaining regions within the mound contour are not associated with distinct low-resistance anomalies. However, TEM data indicate anomalies toward the northwest, underlining the necessity to also sample peripheral regions of potential sites to capture the complete SMS potential.

TAG is arguably the most prominent mound in the study area. Multiple geophysical and geological surveys have focused on the internal mound structure, including the Ocean Drilling Program Leg 158 experiments (e.g., Humphris et al., 1995). As such, the internal structure of TAG is well constrained and serves as a blueprint for estimating mineral potentials for other mounds, where less knowledge about the internal structure and data are available. The CSEM resistivity models of TAG (Figures 10g and 10h) show E-W and N-S transects crossing the mound, respectively. Unfortunately, the towing height during the E-W transect exceeded 100 m above the seafloor, which resulted in inadequate sensitivity for TAG's inferred resistivity structure. However, the N-S profile (Figure 10h) is intriguing, as it supports the asymmetric distribution of mineralization and pore water temperatures presented in previous magnetic and geochemical studies (e.g., Galley et al., 2021; Grant et al., 2018). Moreover, the CSEM resistivity model indicates that a significant resistivity contrast compared to the background basalt may only exist for the massive pyrite, pyrite-anhydrite, pyrite-silica and possibly the pyrite silica units (see Knott et al., 1998).

10.1029/2023GC011250

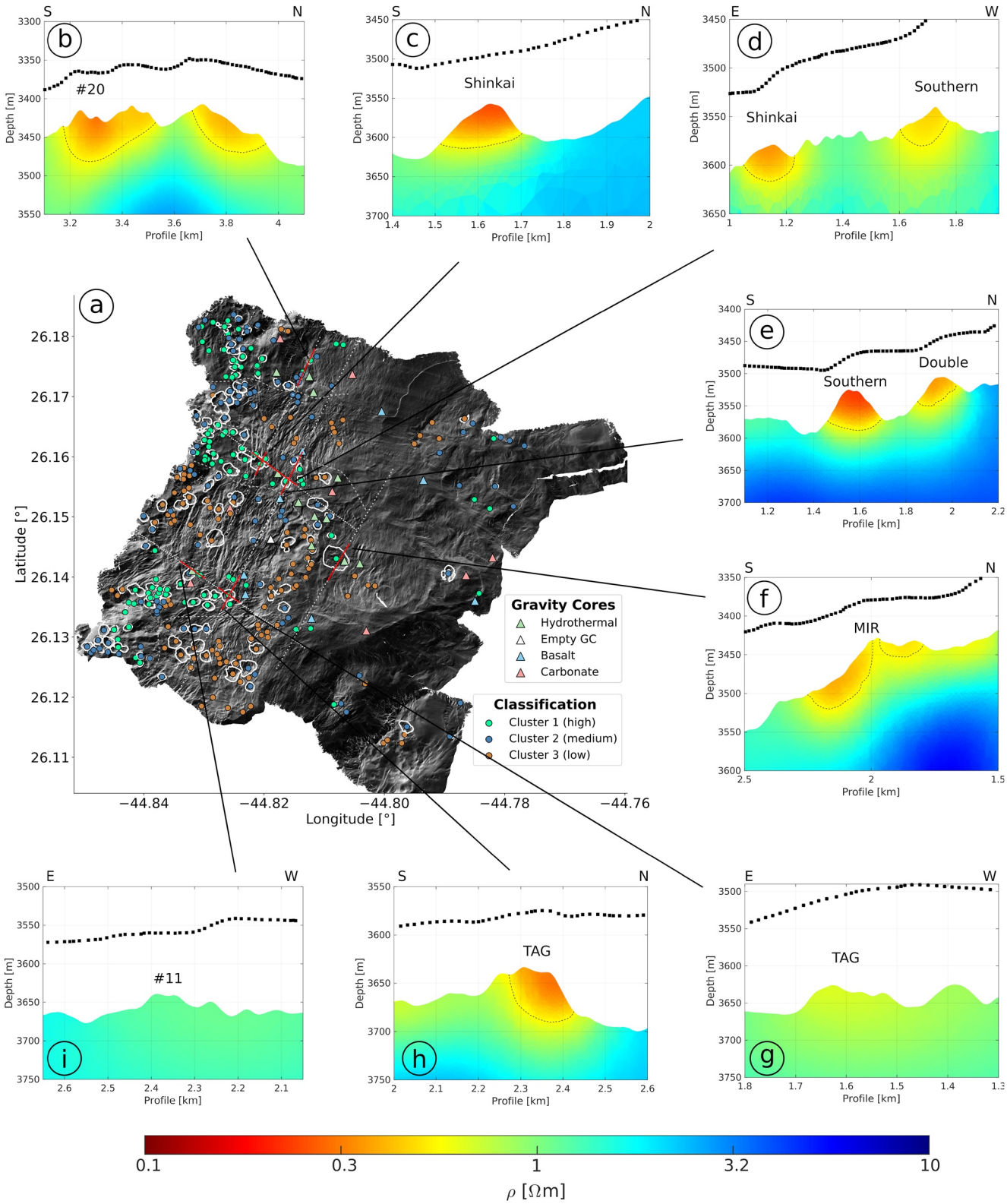

Figure 10. (a) Hillshade bathymetry data with classified mounds as illustrated in Figure 9. Panels (b) through (i) show electrical resistivity models for each of the high priority mounds intersecting a controlled source electromagnetic profile. The lateral extent of each profile is illustrated by red lines in panel (a). In panels (b) through (i), red color shading indicates low resistivity (mineralization), whereas green/blue are more resistive background basalts. Black markers denote transmitter positions along the profile.

Shimmering is the only previously mapped SMS mound in the northern band. However, multiple gravity cores confirm a more hydrothermal activity in the vicinity, which is supported by the CSEM resistivity model (Figure 10b). A prominent resistivity anomaly is not only visible for Shimmering and its adjacent mound, referred to as #20 in Gehrmann et al. (2019) but also along the northern flank of a mound located further north. If this anomaly is induced through mineralization, it needs to be further investigated through visual confirmation and in situ sampling.

5. Discussion

5.1. Automated SMS Mapping Using Machine Learning

The presented workflow can be used as a blueprint for prioritizing SMS exploration targets at mid-ocean ridges and understanding the distributions of mineral potentials. The workflow reduces the total area of interest from the surveyed 49–3.1 km^2, which in turn can be further reduced to either 1.92 km^2 (Clusters 1 and 2) or 0.98 km^2 (only Cluster 1) using additional magnetic constraints. Moreover, the latitudinal bands of hydrothermal activity identified through this integrated analysis reveal prospective areas where further SMS exploration appears sensible, for example, north of Shimmering. The workflow is fully automated, allowing us to identify regions of interest in quasi real-time (if a pre-trained model exists) when new data are acquired, thus, reducing exploration costs considerably and permitting more targeted surveying. Additionally, the workflow is adaptable to future developments in marine mineral exploration and research and its application in other survey areas with similar data layers appears feasible.

The data preparation part of our workflow seeks to unify the bathymetry data acquired at different spatial resolution and at various sites across the globe into a common representation independent of the actual depth, slope, and curvature within a given area. Juliani and Juliani (2021) propose a principal component analysis (PCA) consisting of both a change in slope and a multi-directional shading of elevation data in order to reduce the bathymetric inputs. However, our experience with attempting to use PCA did not generalize well for bathymetry data acquired at different regions with variable roughness and geological strike directions. A key advantage of our proposed processing scheme is notably that bathymetry data from different regions will unify into a coherent visualization. However, further adaptations of this processing step could render it useful to further improve U-Net performance.

Moreover, the workflow is adaptable to test and use other types of ML segmentation tools, and to include additional data layers (e.g., high-resolution backscatter, self-potential, etc.), which may allow for instance or panoptic segmentation. As many of these additional data layers are currently not available in open-access repositories, they can be integrated best within the post-processing step. As backscatter and self-potential data become more readily available (Safipour et al., 2017), it is also feasible to train the U-Net directly for different types of mounds using the co-located spatial data as U-Net input. Such multivariate integration will likely achieve higher certainty in identifying SMS sites.

Following Szitkar et al. (2019) and Rona (1978, 1980), hydrothermal mounds within the TAG field are associated with a distinct negative RTP magnetic anomaly, whereas volcanic edifices typically display positive values. This characteristic proves suitable for clustering depicted mound contours into groups to identify their potential origins. However, three aspects must be considered to integrate the magnetic footprint of a mound or a group of adjacent mounds with the corresponding bathymetry attributes.

1. Magnetic anomaly data are acquired at a lower resolution of 10 m grid spacing compared to the 2 m resolution of the bathymetry data. A pixel-wise comparison between magnetic anomalies and morphological features requires an up-sampling of the magnetic anomaly data, which may lead to interpolation artifacts.
2. An RTP magnetic anomaly shows magnetization and geomagnetic field vectors that render vertical anomalies above the causative body. Szitkar et al. (2019) interpret the vertical negative magnetic anomalies to represent hydrothermal conduits centered above their corresponding source. However, tectonic events can tilt the crustal block, causing altered shapes of the magnetic anomalies, leading to incoherent magnetic anomalies associated with morphological expression. A similar effect is also observable if tectonic forces act on a previously deposited mound.
3. AUV magnetic data are susceptible to errors that arise from inaccuracies in AUV positioning relative to its calibrated coordinates. This may lead to a lateral shift between the morphological expression and the corresponding RTP magnetic anomaly.

All three undetermined circumstances lead to uncertainties in a pixel-wise integration of the magnetic and corresponding bathymetry data. Hence, a relaxation of spatial similarities between mound structures and resulting magnetic anomalies, as we presented here, is required.

Any ML workflow targeting SMS can benefit from a greater number of labeled bathymetry data available in online repositories to improve model training. A significant effort is required to manually label data but is necessary for developing supervised ML workflows. The chosen study area belongs to the most studied hydrothermal sites globally and provides a solid first training set. The developed workflow focuses on the analysis of high-resolution bathymetry data, which resembles the most commonly collected data in seafloor exploration. Given the steady increase in sea-going SMS research, manual assessments of each individual data layer become increasingly difficult and automatization of workflows will be inevitable. Therefore, the application of the workflow in other hydrothermal areas either at mid-ocean ridges or other geological environments with complex and rough terrain is a crucial future task.

5.2. Implications for Hydrothermal Activity in the TAG Area

Notably, marine mineral exploration is a complex endeavor unlikely to be solved using a silver bullet approach. Thus, various ML strategies and conventional geoscientific research will attest the feasibility of detecting SMS and estimating mineral potentials. The proposed ML strategy does not contradict this notion, but instead offers an avenue for methodological development seeking to integrate multivariate data sets into a common interpretation that is easily manually audited. Note that the delineation of convex structures in bathymetry data underlies some variability resulting from terrain analysis and, even if conducted manually, remains ambiguous due to interfering geomorphic processes that mask or distort typical mound morphologies. Hence, although mapping the correct mound dimensions is significant for addressing mineral potentials, discrepancies between manual and automated segmentation are expected.

Despite these explainable deviations, the spatial alignment of Cluster 1 bands is clearly visible and the correlation to structural domains defined by Graber et al. (2020) is apparent. This may support the hypotheses of a structural heterogeneity within the hydrothermal field dictating the distribution of SMS edifices, as proposed by Graber et al. (2020). Both the spatial extent of the alignment and the occurrence of deviating areas indicate a structural constraint in the deep subsurface. This dominant structural constraint supports an interpretation where a strongly distorted subsurface structuring (e.g., bended detachment fault) leads to focused fluid flow in the deep subsurface that results in a linear, off-axis distribution of hydrothermal edifices. Moreover, the various upflow zones are likely to span a region larger than the investigated area of study. Further sites may be located north of Shimmering and also south of TAG, as well as in the ridgeward extension of the three bands. Conclusively, the presented workflow has demonstrated a successful amalgamation of bathymetry and geophysical data, which could be used to inform future SMS research and exploration studies.

The number of potential SMS sites drastically increased through this automated workflow. However, geophysical analysis indicates that mineral potentials at the known sites are likely lower than originally presumed. EM data combined with in situ samples illustrates that mineralized zones can be heterogeneously distributed across the mound contour, thus, significantly reducing the proposed tonnage estimates. MIR for example, appears to be heterogeneous and more resistive compared to other known sites, which could imply that mineral predictions are overestimated. To improve these estimates in future work, we propose that SMS exploration requires a combination of seafloor drilling and additional data layers such as self-potential, backscatter, magnetics, seismics, and 3D resistivity models to capture the heterogeneity of SMS mounds and achieve a high degree of certainty in mineral predictions. If such high-resolution survey strategies are economical, this remains beyond the scope of this study.

It cannot be ruled out that future endeavors may potentially change the presented prioritization of SMS mounds in the TAG region through more discoveries or through the acquisition of additional data layers. It is expected that not all mounds within Cluster 1 are associated with SMS edifices and that additional data will improve the certainty of the automated SMS prediction. Overall, a more diversified data set measured at numerous SMS sites across the global MORs will only help improve our understanding of SMS predictors and improve future ML developments.

Marine CSEM and TEM data integrated into a multi-physics approach provide additional value to understand the internal structure, pore fluid temperature distribution and potential mineralization of SMS edifices. However,

more development is required to improve the depth penetration and sensitivity of CSEM surveys targeting SMS. The applied CSEM configuration appears susceptible to signal attenuation and distortions in these conductive settings with rough seafloor topography. Problems concerning safe towing altitudes and limited depth of penetration are known obstacles. Adaptations that combine seafloor EM nodes and towed receiver arrays can likely help mitigate sensitivity issues as demonstrated in other fields of CSEM research (e.g., Attias et al., 2018). Alternatively, the greatest potential of imaging spatially-confined targets such as SMS using CSEM may lie in the use of AUVs. An AUV or a fleet of AUVs could acquire numerous transmitter-receiver configurations and offsets across a spatially confined SMS area. This will help to accurately derive 3D resistivity models of SMS sites including peripheral regions in these remote settings. MacGregor et al. (2021) have presented a first attempt of a 3D CSEM AUV experiment targeting SMS and others are likely to follow suit.

6. Conclusion

A workflow to conduct automated SMS site detection using multivariate geoscientific data is presented that employs a U-Net convolutional neural network to identify prominent mound-like morphologies in bathymetry data. The predicted contours are subsequently integrated with other spatial data layers (e.g., AUV magnetic data) to identify potential sites for future SMS prospecting studies. Within the 49 km^2 grid of high-resolution bathymetry data, 323 mounds were detected. Ninety-eight of which were classified as high priority due to their architecture and magnetic signature. Moreover, from the automated analysis 14 of the 15 known SMS sites in the TAG area were identified as either high (10) or medium (4) priority. Only one known site was classified within the low-priority group. The high-priority sites are spatially distributed along latitudinal bands, supporting the hypothesis that focused fluid-flow at depth leads to linear distributions of off-axis SMS edifices in the area.

The presented workflow cannot only be used to improve the analysis and interpretation of previously surveyed areas but also serve as a blueprint to optimize the SMS exploration at sea. The trained model can be applied to newly acquired bathymetry data in quasi real-time to determine prospective zones for more detailed confirmation/visualization studies. Thus, optimizing the use of ship time and reducing exploration costs. The workflow is very adaptable to include additional data layers such as backscatter, self-potential, turbidity and other available data maps.

Electrical resistivity models combined with in situ rock sampling demonstrate that mineralization can be distributed less homogeneously than previously considered. High mineral grades observed at specific points on a mound are not necessarily distributed across the mound volume. Thus, mineral potentials for SMS can be significantly overestimated. Consequently, although the workflow detects many more potential SMS edifices than previously classified, the individual resource potential at confirmed SMS sites is likely lower than previously estimated.

Appendix A

Table A1
List of Open-Access Bathymetry Data Used for Training the U-Net

Index	Extent: Longitude min. / Longitude max.	Extent: Latitude min. / Latitude max	Resolution	Source/reference
1	−44.99625 / −44.69042	25.98625 / 26.28625	~90 m	Multibeam Mosaic https://www.ncei.noaa.gov/maps/bathymetry/
2	−43.23542 / −41.31541	29.69375 / 30.78042	~90 m	Multibeam Mosaic https://www.ncei.noaa.gov/maps/bathymetry/
3	−34.45958 / −33.12792	35.45792 / 37.50708	~90 m	Multibeam Mosaic https://www.ncei.noaa.gov/maps/bathymetry/
4	−27.14292 / −23.76958	61.70625 / 63.44625	~90 m	Multibeam Mosaic https://www.ncei.noaa.gov/maps/bathymetry/

Table A1
Continued

Index	Extent: Longitude min. / Longitude max.	Extent: Latitude min. / Latitude max	Resolution	Source/reference
5	−45.21799 / −44.40485	25.77404 / 26.54754	~30 m	Petersen (2019) https://doi.org/10.1594/PANGAEA.899415
6	−44.85162 / −44.75758	26.10058 / 26.18684	~2 m	Petersen (2019) https://doi.org/10.1594/PANGAEA.899415
7	−44.97116 / −44.86794	13.27914 / 13.34156	~2m	Escartín and Petersen (2017) and Escartin et al. (2017)
8	−45.00966 / −44.88124	13.48664 / 13.52226	~2 m	Escartín and Petersen (2017) and Escartin et al. (2017)
9	−46.45929 / −45.81298	22.36806 / 23.05779	~10 m	Villinger et al. (2018) https://doi.org/10.1594/PANGAEA.889439
10	−34.99333 / −31.87833	56.69666 / 58.00000	~90 m	Multibeam Mosaic https://www.ncei.noaa.gov/maps/bathymetry/
11	−42.40119 / −41.72925	29.82935 / 30.36156	~90 m	Multibeam Mosaic https://www.ncei.noaa.gov/maps/bathymetry/
12	−129.1490 / −129.0070	47.88199 / 48.08900	~1 m	Clague et al. (2015)http://get.iedadata.org/doi/321990
13	−177.1383 / −176.3533	−23.0983 / −21.5792	~90 m	Multibeam Mosaic https://www.ncei.noaa.gov/maps/bathymetry/
14	−29.93012 / −22.78952	35.99997 / 39.50023	~45 m	Hübscher and Beier (2022) https://doi.pangaea.de/10.1594/PANGAEA.945528

Data Availability Statement

The bathymetry data used for training the U-Net model are available on open-access repositories as listed in Table A1. The AUV-bathymetry and magnetic anomaly maps are available from Petersen (2019) and CSEM data from Gehrmann (2019).

Acknowledgments
We would like to thank two anonymous reviewers and Marie Edmonds for their insightful comments that helped us improve our paper. AH was in part funded by the Digital Earth and Sustainable Management of Offshore Groundwater Resources (SMART) Projects at GEOMAR Helmholtz Centre of Ocean Research Kiel. We would like to thank the European Commission for funding the Framework 7 project Blue Mining (Grant 604500). We thank all cruise participants and crew from M127 and JC138 for their support in data acquisition. We thank Kerry Key for the inversion code MARE2DEM and supporting MATLAB scripts as well as David Myer for processing the routines. Open Access funding enabled and organized by Projekt DEAL.

References

Ade-Hall, J. M., Palmer, H. C., & Hubbard, T. P. (1971). The magnetic and opaque petrological response of basalt to regional hydrothermal alteration. *Geophysical Journal of the Royal Astronomical Society*, *24*(2), 137–174. https://doi.org/10.1111/j.1365-246x.1971.tb02171.x

Andersen, C., Rüpke, L., Hasenclever, J., Grevemeyer, I., & Petersen, S. (2015). Fault geometry and permeability contrast control vent temperatures at the Logatchev 1 hydrothermal field, Mid-Atlantic Ridge. *Geology*, *43*(1), 51–54. https://doi.org/10.1130/G36113.1

Attias, E., Weitemeyer, K., Hölz, S., Naif, S., Minshull, T. A., Best, A. I., et al. (2018). High-resolution resistivity imaging of marine gas hydrate structures by combined inversion of CSEM towed and ocean-bottom receiver data. *Geophysical Journal International*, *214*(3), 1701–1714. https://doi.org/10.1093/gji/ggy227

Beaulieu, S. E., Baker, E. T., & German, C. R. (2015). Where are the undiscovered hydrothermal vents on oceanic spreading ridges? *Deep-Sea Research Part II Topical Studies in Oceanography*, *121*, 202–212. https://doi.org/10.1016/j.dsr2.2015.05.001

Beaulieu, S. E., Baker, E. T., German, C. R., & Maffei, A. (2013). An authoritative global database for active submarine hydrothermal vent fields. *Geochemistry, Geophysics, Geosystems*, *14*(11), 4892–4905. https://doi.org/10.1002/2013GC004998

Beaulieu, S. E., & Szafranski, K. (2020). InterRidge global database of active submarine hydrothermal vent fields. Version 3.4. World Wide Web electronic publication. Retrieved from http://vents-data.interridge.org

Bouwer, L. M., Dransch, D., Ruhnke, R., Rechid, D., Frickenhaus, S., & Greinert, J. (2022). In L. M. Bouwer, D. Dransch, R. Ruhnke, D. Rechid, S. Frickenhaus, & J. Greinert (Eds.), *Integrating data science and earth science: Challenges and solutions*. Springer Nature. https://doi.org/10.1007/978-3-030-99546-1

Clague, D., Dreyer, B. M., Paduan, J. B., Martin, J. F., Caress, D. W., Gill, J. B., et al. (2015). Processed near-bottom Sidescan Sonar Data (version 2) from the Juan de Fuca Spreading Center - Endeavour Segment acquired with AUV D. Allan B. during the Zephyr expedition ZPR1108 (2011). *Interdisciplinary Earth Data Alliance (IEDA)*. https://doi.org/10.1594/IEDA/321990

Constable, S., Kannberg, P. K., & Weitemeyer, K. (2016). Vulcan: A deep-towed CSEM receiver. *Geochemistry, Geophysics, Geosystems*, *17*(3), 1042–1064. https://doi.org/10.1002/2015GC006174

Constable, S., Kowalczyk, P., & Bloomer, S. (2018). Measuring marine self-potential using an autonomous underwater vehicle. *Geophysical Journal International*, *215*(1), 49–60. https://doi.org/10.1093/gji/ggy263

Escartin, J., Mevel, C., Petersen, S., Bonnemains, D., Cannat, M., Andreani, M., et al. (2017). Tectonic structure, evolution, and the nature of oceanic core complexes and their detachment fault zones (13°20′N and 13°30′N, Mid-Atlantic Ridge). *Geochemistry, Geophysics, Geosystems*, *18*(4), 1451–1482. Publisher's official version. https://doi.org/10.1002/2016GC006775

Escartín, J., & Petersen, S. (2017). ODEMAR AUV Abyss (GEOMAR) + shipboard Pourquoi Pas? Multibeam bathymetry – 13deg20′N and 13deg30′N oceanic core complexes, mid Atlantic Ridge. *SEANOE*. https://doi.org/10.17882/48335

Fouquet, Y., Cambon, P., Etoubleau, J., Charlou, J. L., Ondreas, H., Barriga, F. J. A. S., et al. (2010). Geodiversity of hydrothermal processes along the Mid-Atlantic Ridge and ultramafic-hosted mineralization: A new type of oceanic Cu-Zn-Co-Au volcanogenic massive sulfide deposit. *Geophysical Monograph Series*, *188*, 321–367.

Galley, C., Lelièvre, P., Haroon, A., Graber, S., Jamieson, J., Szitkar, F., et al. (2021). Magnetic and gravity surface geometry inverse modeling of the TAG active mound. *Journal of Geophysical Research: Solid Earth*, *126*(10), e2021JB022228. https://doi.org/10.1029/2021JB022228

Gazis, I.-Z., Schoening, T., Alevizos, E., & Greinert, J. (2018). Quantitative mapping and predictive modeling of Mn nodules' distribution from hydroacoustic and optical AUV data linked by random forests machine learning. *Biogeosciences*, *15*(23), 7347–7377. https://doi.org/10.5194/bg-15-7347-2018

Gehrmann, R., North, L. J., Graber, S., Szitkar, F., Petersen, S., Minshull, T. A., & Murton, B. J. (2019). Marine mineral exploration with controlled source electromagnetics at the TAG hydrothermal field, 26° N Mid-Atlantic Ridge. *Geophysical Research Letters*, *46*(11), 5808–5816. https://doi.org/10.1029/2019GL082928

Gehrmann, R. A. S. (2019). Controlled-source electromagnetic data from the TAG hydrothermal field, 26N Mid-Atlantic Ridge [Dataset]. PANGAEA. https://doi.org/10.1594/PANGAEA.899073

Gehrmann, R. A. S., Haroon, A., Morton, M., Djanni, A. T., & Minshull, T. A. (2020). Seafloor massive sulphide exploration using deep-towed controlled source electromagnetics: Navigational uncertainties. *Geophysical Journal International*, *220*(2), 1215–1227. https://doi.org/10.1093/gji/ggz513

Graber, S., Petersen, S., Yeo, I., Szitkar, F., Klischies, M., Jamieson, J., et al. (2020). Structural control, evolution, and accumulation rates of massive sulfides in the TAG hydrothermal field. *Geochemistry, Geophysics, Geosystems*, *21*(9), e2020GC009185. https://doi.org/10.1029/2020GC009185

Grant, H. L. J., Hannington, M. D., Petersen, S., Frische, M., & Fuchs, S. H. (2018). Constraints on the behavior of trace elements in the actively-forming TAG deposit, Mid-Atlantic Ridge, based on LA-ICP-MS analyses of pyrite. *Chemical Geology*, *498*, 45–71. https://doi.org/10.1016/j.chemgeo.2018.08.019

Hannington, M., Jamieson, J. W., Monecke, T., Petersen, S., & Beaulieu, S. (2011). The abundance of seafloor massive sulfide deposits. *Geology*, *39*(12), 1155–1158. https://doi.org/10.1130/G32468.1

Haroon, A., Hölz, S., Gehrmann, R. A. S., Attias, E., Jegen, M., Minshull, T. A., & Murton, B. J. (2018). Marine dipole–dipole controlled source electromagnetic and coincident-loop transient electromagnetic experiments to detect seafloor massive sulphides: Effects of three-dimensional bathymetry. *Geophysical Journal International*, *215*(3), 2156–2171. https://doi.org/10.1093/gji/ggy398

Honsho, C., Ura, T., & Kim, K. (2013). Deep-sea magnetic vector anomalies over the Hakurei hydrothermal field and the Bayonnaise knoll caldera, Izu-Ogasawara arc, Japan. *Journal of Geophysical Research: Solid Earth*, *118*(10), 5147–5164. https://doi.org/10.1002/jgrb.50382

Hu, F., Xia, G.-S., Hu, J., & Zhang, L. (2015). Transferring deep convolutional neural networks for the scene classification of high-resolution remote sensing imagery. *Remote Sensing*, *7*(11), 14680–14707. https://doi.org/10.3390/rs71114680

Hübscher, C., & Beier, C. (2022). Multibeam bathymetry processed data (EM 120 echosounder & Kongsberg EM 122 dataset compilation) of RV METEOR during cruise M79/2, M113/1 & M128, Azores Plateau between the Terceira Rift and the East Azores Fracture Zone, North Atlantic Ocean. *PANGAEA*. https://doi.org/10.1594/PANGAEA.945528

Humphris, S. E., Herzig, P. M., Miller, D. J., Alt, J. C., Becker, K., Brown, D., et al. (1995). The internal structure of an active sea-floor massive sulphide deposit. *Nature*, *377*(6551), 713–716. https://doi.org/10.1038/377713a0

Ishizu, K., Goto, T., Ohta, Y., Kasaya, T., Iwamoto, H., Vachiratienchai, C., et al. (2019). Internal structure of a seafloor massive sulfide deposit by electrical resistivity tomography, Okinawa Trough. *Geophysical Research Letters*, *46*(20), 11025–11034. https://doi.org/10.1029/2019GL083749

Jamieson, J. W., Clague, D. A., & Hannington, M. D. (2014). Hydrothermal sulfide accumulation along the Endeavour Segment, Juan de Fuca Ridge. *Earth and Planetary Science Letters*, *395*, 136–148. https://doi.org/10.1016/j.epsl.2014.03.035

Jamieson, J. W., & Gartman, A. (2020). Defining active, inactive, and extinct seafloor massive sulfide deposits. *Marine Policy*, *117*, 103926. https://doi.org/10.1016/j.marpol.2020.103926

Juliani, C., & Juliani, E. (2021). Deep learning of terrain morphology and pattern discovery via network-based representational similarity analysis for deep-sea mineral exploration. *Ore Geology Reviews*, *129*, 103936. https://doi.org/10.1016/j.oregeorev.2020.103936

Keohane, I., & White, S. (2022). Chimney identification tool for automated detection of hydrothermal chimneys from high-resolution bathymetry using machine learning. *Geosciences*, *12*(4), 176. https://doi.org/10.3390/geosciences12040176

Key, K. (2016). MARE2DEM: A 2-D inversion code for controlled-source electromagnetic and magnetotelluric data. *Geophysical Journal International*, *207*(1), 571–588. https://doi.org/10.1093/gji/ggw290

Knott, R., Fouquet, Y., Honnorez, J., Pertersen, S., & Bohn, M. (1998). Petrology of hydrothermal mineralization: A vertical section through the TAG mound. *Proceedings of the Ocean Drilling Program: Scientific Results*, *158*, 5–26. https://doi.org/10.2973/odp.proc.sr.158.201.1998

Koedel, U., Dietrich, P., Fischer, P., Greinert, J., Bundke, Burwicz-Galerne, E., et al. (2022). The digital Earth smart monitoring concept and tools. In L. M. Bouwer, D. Dransch, R. Ruhnke, D. Rechid, S. Frickenhaus, & J. Greinert (Eds.), *Integrating data science and earth science. SpringerBriefs in earth system sciences*. Springer. https://doi.org/10.1007/978-3-030-99546-1_6

MacGregor, L., Kowalcyk, P., Galley, C., Weitemeyer, K., Bloomer, S., Phillips, N., & Proctor, A. (2021). Characterization of seafloor mineral deposits using multiphysics datasetes acquired from an AUV. *First Break*, *39*(8), 63–69. https://doi.org/10.3997/1365-2397.fb2021062

Mikolajczjk, A., & Grochowski, M. (2018). Data augmentation for improving deep learning in image classification problem. In *2018 international interdisciplinary PhD workshop (IIPhDW)* (pp. 117–122). https://doi.org/10.1109/IIPHDW.2018.8388338

Morgan, L. A. (2012). Geophysical characteristics of volcanogenic massive sulfide deposits. In W. C. Pat Shanks, III & R. Thurston (Eds.), *Volcanogenic sulfide occurrence model* (pp. 115–131). USGS.

Müller, H., Schwalenberg, K., & Barckhausen, U. (2023). Magnetic and electromagnetic exploration of SMS deposits; perspectives and frontiers. In *84th EAGE Annual Conference & Exhibition, 2023* (pp. 1–5). https://doi.org/10.3997/2214-4609.2023101269

Murton, B. J., Lehrmann, B., Dutrieux, A. M., Martins, S., Gil de la Iglesia, A., Stobbs, I. J., et al. (2019). Geological fate of seafloor massive sulphides at the TAG hydrothermal field (Mid-Atlantic Ridge). *Ore Geology Reviews*, *107*, 903–925. https://doi.org/10.1016/j.oregeorev.2019.03.005

Murton, B. J., & Shipboard (2018). *Cruise report: Expedition JC138: 29th June–8th August 2016, mid Atlantic Ridge, 26°8.38'N; 44°49.92'W* (p. 285). National Oceanography Centre Southampton. Scientific Party. Retrieved from https://www.bodc.ac.uk/resources/inventories/cruise_inventory/reports/jc138.pdf

Olakunle, O. K., Ajibola, L. M., Muhammad, I. H., & Makovsky, Y. (2021). Massive seafloor mounds depict potential for seafloor mineral deposits in the Great South Basin (GSB) offshore New Zealand. *Scientific Reports*, *11*(1), 9185. https://doi.org/10.1038/s41598-021-88620-x

Petersen, S., & Shipboard Scientific Party. (2016). *RV METEOR cruise report M127 metal fluxes and resource potential at the slow-spreading TAG midocean ridge segment (26°N, MAR) – Blue Mining@Sea, Bridgetown (Barbados) – Ponta Delgada (Portugal), 25.05.–28.06.2016*. GEOMAR Report, N. Ser. 032 (Vol. 87, p. 69). GEOMAR Helmholtz-Zentrum für Ozeanforschung Kiel. https://doi.org/10.3289/GEOMAR_REP_NS_32_2016

Petersen, S. (2019). Bathymetric data products from AUV dives during METEOR cruise M127 (TAG Hydrothermal Field, Atlantic). [Dataset]. GEOMAR - Helmholtz Centre for Ocean Research Kiel. PANGAEA. https://doi.org/10.1594/PANGAEA.899415

Reeck, K., Müller, H., Hölz, S., Haroon, A., Schwalenberg, K., & Jegen, M. (2020). Effects of metallic system components on marine electromagnetic loop data. *Geophysical Prospecting*, *68*(7), 2254–2270. https://doi.org/10.1111/1365-2478.12984

Rona, P. A. (1978). Criteria for recognition of hydrothermal mineral deposits in oceanic crust. *Economic Geology*, *73*(2), 135–160. https://doi.org/10.2113/gsecongeo.73.2.135

Rona, P. A. (1980). TAG hydrothermal field: Mid-Atlantic Ridge crest at latitude 26°N. *Geological Society of London Journal*, *137*(4), 385–402. https://doi.org/10.1144/gsjgs.137.4.038

Ronneberger, O., Fischer, P., & Brox, T. (2015). U-Net: Convolutional networks for biomedical image segmentation. In N. Navab, J. Hornegger, W. Wells, & A. Frangi (Eds.), *Medical image computing and computer-assisted intervention – MICCAI 2015*. MICCAI 2015, *Lecture notes in computer science* (Vol. 9351). Springer. https://doi.org/10.1007/978-3-319-24574-4_28

Safipour, R., Hölz, S., Halbach, J., Jegen, M., Petersen, S., & Swidinsky, A. (2017). A self-potential investigation of submarine massive sulfides: Palinuro Seamount, Tyrrhenian Sea. *Geophysics*, *82*(6), A51–A56. https://doi.org/10.1190/geo2017-0237.1

Sinha, M. C., Patel, P. D., Unsworth, M. J., Owen, T. R. E., & Maccormack, M. R. G. (1990). An active source electromagnetic sounding system for marine use. *Marine Geophysical Researches*, *12*(1–2), 59–68. https://doi.org/10.1007/BF00310563

Spagnoli, G., Hannington, M., Bairlein, K., Hördt, A., Jegen, M., Petersen, S., & Laurila, T. (2016). Electrical properties of seafloor massive sulfides. *Geo-Marine Letters*, *36*(3), 235–245. https://doi.org/10.1007/s00367-016-0439-5

Swidinsky, A., Hölz, S., & Jegen, M. (2012). On mapping seafloor mineral deposits with central loop transient electromagnetics. *Geophysics*, *77*(3), E171–E184. https://doi.org/10.1190/geo2011-0242.1

Szitkar, F., Dyment, J., Petersen, S., Bialas, J., Klischies, M., Graber, S., et al. (2019). Detachment tectonics at Mid-Atlantic Ridge 26°N. *Scientific Reports*, *9*(1), 11830. https://doi.org/10.1038/s41598-019-47974-z

Villinger, H., Strack, A., Gaide, S., & Thal, J. (2018). Gridded bathymetry of North Pond (MAR) from multibeam echosounder EM120 and EM122 data of cruises MSM20/5 (2012) and MSM37 (2014). Department of Geosciences, Bremen University. *PANGAEA*. https://doi.org/10.1594/PANGAEA.889439